Microstructural evolution of Fe–20Cr–30Ni–2Nb–5Al AFA steel during creep at 760 °C

Andrew Peterson, Ian Baker[*]

Thayer School of Engineering, Dartmouth College, Hanover, NH, 03755, USA

ABSTRACT

The microstructural evolution of an alumina-forming austenitic stainless-steel Fe–20Cr–30Ni–2Nb–5Al (at. %) was investigated after creep at 760 °C. It was found that the secondary creep rate was correlated with changes in the microstructure. During creep, both Laves phase and B2 precipitates in the matrix both coarsened and increased in volume fraction. In addition, nano-sized $L1_2$-structured Ni_3Al precipitates nucleated and then coarsened and increased in volume fraction during creep. Grain boundary coverage by Laves phase and B2 precipitates increased during creep, and a precipitate free zone (PFZ) formed along the grain boundaries at creep times great than 2000 h. The creep rate decreased for times up to ~2000 h primarily due to strengthening from the $L1_2$ precipitates, with grain boundary strengthening playing a minor role. At longer times, there was a slight increase in creep rate, due to the coarsening of precipitates in the matrix and the formation of the PFZ.

1. Introduction

Despite the surge of renewable energy, fossil fuels are likely to remain the primary energy source for the near future. Therefore, it is important to use these resources as efficiently as possible – both for economic reasons and in order to minimize pollutants such as CO_2 [1,2]. Currently, the martensitic and ferritic alloys which are being used in fossil-fuel power plants are limited to operating temperatures of less than 600 °C [2]. The US Department of Energy has set a goal to develop materials technology to enable the operation of power plants with steam at 760 °C and 35 MPa [1,3]. Achieving this goal can reduce emissions (including CO_2) from the current fleet of power plants in the US by up to 20% [1,3]. This will require a material that is strong, displays good oxidation and corrosion resistance, and is economically viable [1]. Nickel-based superalloys can satisfy most of these requirements – but these materials are too expensive for use in energy applications [4]. AFAs (alumina forming austenitic stainless steels) are a promising new class of steels with potential to meet all of the above requirements [5–8].

AFAs have primarily been under development at Oak Ridge National Lab [5,6,8–12]. They use alumina as a protective oxide scale for high corrosion resistance because this offers better protection than chromia [13,14]. The latest family of AFAs is strengthened with laves phases [4, 8–10]. These AFAs also use a "grain boundary (GB) precipitation strengthening mechanism" [15]. In this newer family of AFAs, B2

structured NiAl and Fe_2Nb Laves phase precipitates exist both in the austenitic matrix and on the GBs. There are also either MC precipitates or $L1_2$ structured Ni_3Al-based precipitates present in the matrix that increase the creep strength [10–12]. Recent work has been performed to understand the high temperature mechanical properties of AFAs. Several studies have been performed to understand the plastic flow behavior of AFAs, which have found that the high temperature deformation behavior can be described well by a power law model using a threshold stress term for the precipitates [16,17]. Additionally, studies have found that the strength is generally controlled by nano-sized $L1_2$ precipitates or carbides [16,18]. A recent creep study performed at 700 °C and 150 MPa or 240 MPa on an AFA alloy which contained Laves phase, B2, $L1_2$, $M_{23}C_6$ carbide, and MC carbide precipitates found that the $L1_2$ matrix precipitates showed Ostwald ripening with the size increase proportional to $t^{1/3}$; a precipitate free zone (PFZ) that increased in size proportional to $t^{1/2}$; and that the B2 precipitates on the GB show a linear size increase with time [19]. Additionally, the $M_{23}C_6$ carbides, which were located mainly on the GB, rapidly increased in size from nano-sized to micron-sized. The study found that the failure mode for the 240 MPa test was transgranular, while the failure mode for the 150 MPa test was intergranular. The researchers suggested that this change in failure modes means that the GBs weakened quicker than the grain interior, likely due to the growth of the PFZ and coarsening of precipitates along the GB.

---

* Corresponding author.
E-mail address: ian.baker@dartmouth.edu (I. Baker).

The present study was performed on the AFA model alloy Fe–20Cr–30Ni–2Nb–5Al (at. %) [20–23]. This alloy contains B2 NiAl precipitates and Laves phase Fe₂Nb precipitates both in the matrix and along the GB after annealing at elevated temperatures. L1$_2$ structured Ni$_3$Al precipitates also form in the matrix, but only below ~800 °C. Another interesting feature of the microstructure is that a precipitate free zone (PFZ) forms along the grain boundaries at long annealing times [20–22]. A model of what the microstructure would look like after creep is shown in Fig. 1. Baker et al. performed preliminary creep tests and high temperature tensile tests on this alloy at 760 °C after a variety of anneals, viz., solutionized, annealed for 2.4 h at 800 °C, annealed for 24 h at 800 °C, and annealed for 240 h at 800 °C [20]. There were several interesting observations from this research:

1. The specimen annealed for 2.4 h displayed the lowest creep strain. This anneal resulted in fine Laves phase precipitates in the matrix and GB coverage of 42% by Laves and B2 phase precipitates prior to creep testing.
2. The 24 h annealed specimen showed a larger strain primary creep strain, but exhibited a similar secondary creep rate to the 2.4 h annealed specimen. This 24 h anneal produced similarly sized matrix precipitates to the 2.4 h annealed specimen but had significantly larger GB coverage (69%). It was, thus, suggested the GB coverage either does not affect the creep rate or that 42% GB coverage is sufficient to prevent GB sliding.
3. Both the 240 h annealed specimen, which had much larger matrix precipitates, and the solutionized specimen displayed much worse creep strength than both the 2.4 h and 24 h annealed specimens. This suggests that fine Laves and B2 precipitates are beneficial to creep strength, but as these precipitates coarsen they become deleterious to creep strength.
4. While none of the anneals contained L1$_2$ precipitates prior to creep, the L1$_2$ precipitates nucleated and grew during the creep tests at 760 °C. All anneals showed similar L1$_2$ precipitate size and volume fraction after creep, making it difficult to discern the effect of these precipitates on creep rate.
5. The creep rates appeared to be roughly constant throughout secondary creep even though the microstructure evolved during the testing.

The current research on AFAs shows that the microstructure of the alloy evolves significantly during creep. Additionally, the size, spacing, and GB coverage of precipitates has been shown to have a significant effect on the high temperature strength of AFA alloys. Thus, it is likely that the microstructure evolution during creep affects the creep strength of the alloy. In this paper, we present a study of the microstructure evolution of Fe–20Cr–30Ni–2Nb–5Al during creep and the effect that this evolution has on the creep rate. Additionally, we analyze the deformation mechanisms and fit the deformation behavior to models explaining the behavior as the microstructure evolves. The creep tests in
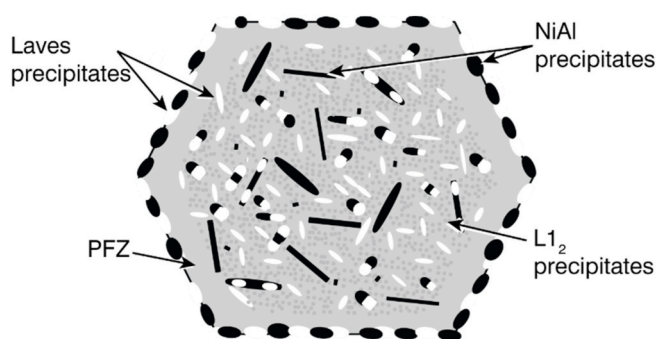
this study are performed on specimens that showed the best creep strength from the preliminary tests, i.e. the 2.4 h 800 °C annealed material [20].

2. Experimental

Fe–20Cr–30Ni–2Nb–5Al (at. %) was cast into an 8 kg ingot using split-cast vacuum induction by Carpenter Technology Corporation. The ingot was press-forged in 19 mm × 19 mm x 600 mm rectangular bars. The alloy was solutionized by annealing in an argon atmosphere for 24 h at 1250 °C. Previous research on this alloy showed that this heat treatment results in a single phase microstructure [22].

Creep specimens were milled into dog-bone tensile specimens with gauge cross-sections dimensions of 2.7 mm × 2 mm and a gauge length of 20 mm. The tensile specimens were annealed for 2.4 h at 800 °C in air, and air cooled. The specimens were polished with successively finer silicon carbide paper up to 1200 grit, and then further polished with 0.3 μm and 0.05 μm alumina powder to a mirror finish. All creep tests were performed at 760 °C on home-built constant-stress creep jigs based on a design by Garofolo, Richmond, and Domis [24].

Transmission electron microscope (TEM) samples were prepared by cutting 3 mm dia cylinders from specimens using an electro discharge machine. These cylinders were sliced into discs and polished with silicon carbide paper to a thickness of ~100 μm. Next, the discs were electro-polished using 20% nitric acid in methanol at temperatures of −40 °C to −20 °C at 11 V and a flow rate of 15 in a Struer Tenupol 5. After electropolishing, the TEM specimens were alternately rinsed in ethanol and methanol solutions three times. Imaging was performed on a FEI Tecnai F20 FEG TEM operated at 200 kV using a low-background double-tilt holder. ImageJ was used to analyze the TEM images. Circles were manually drawn over the L1$_2$ precipitates in order to measure their size. Average diameter and volume fraction were determined. The volume fraction was calculated by determining the thickness of the TEM foils using convergent beam electron diffraction (CBED). Three images were analyzed for each condition and a 95% confidence interval was used to calculate the error bars. The L1$_2$ precipitates were identified using TEM diffraction patterns in a previous study of this alloy [20].

Scanning electron microscope (SEM) images were taken from the electropolished area around the hole of the TEM samples. Imaging was performed on a FEI (Thermo Fisher Scientific) Helios 5CX dual beam field emission gun (FEG) SEM. Using a backscattered electron (BSE) detector, the Laves phase precipitates show as light and the B2 phase precipitates show as dark. These precipitates were identified in prior work on this alloy using X-ray diffraction, EDS, and TEM diffraction patterns [22,23]. Image analysis was performed on SEM images using ImageJ. The particle analysis tool was used to determine the size of the Laves and B2 particles by setting the threshold to include only light or dark precipitates. An equivalent diameter was calculated for the average size to allow for easy comparison. Volume fraction was also calculated. Particles that were less than 80 nm in equivalent diameter were ignored because they did not always represent the precipitates. Because of this, the average size calculations does not account for some of the smaller precipitates. Three images were analyzed for each condition. A 95% confidence interval was used to calculate the error.

3. Results

Creep tests were performed at 760 °C at: 35 MPa for 2000 h, 45 MPa for up to 4000 h, 65 MPa for 4000 h, and 75 MPa until failure (4921 h) on material that had been homogenized and then annealed for 2.4 h at 800 °C. This condition has shown the best creep resistance in preliminary testing [20]. The resulting creep curves are shown in Fig. 2, where the higher creep rates at higher stress are clearly evident.

In order to gain an understanding of the microstructural evolution during creep, tests were run at 45 MPa for different time lengths, i.e. 250 h, 500 h, 1000 h, 2000 h, and 4000 h. Each of the resulting creep curves
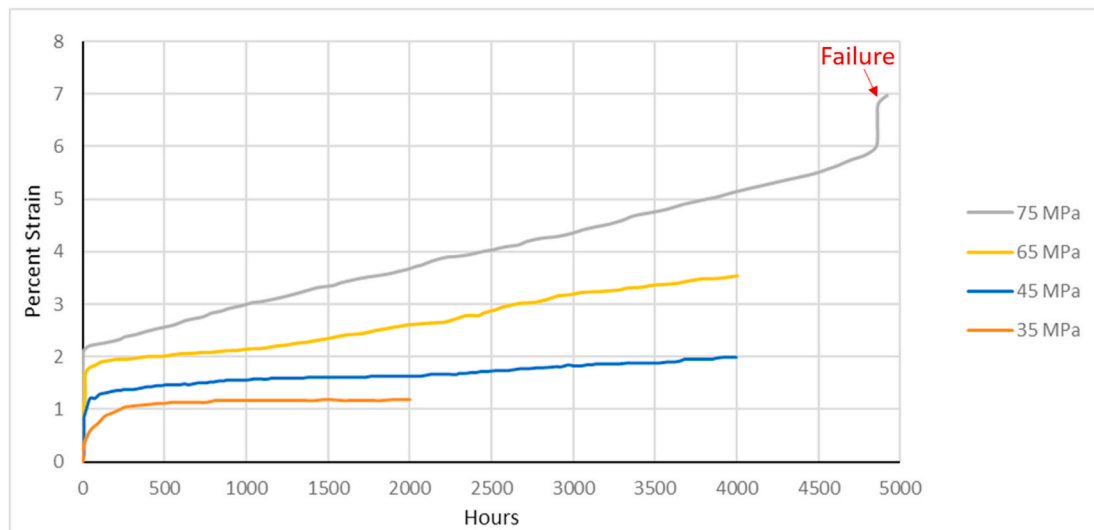

Fig. 1. Schematic of the microstructure of Fe–20Cr–30Ni–2NNb–5Al after creep at 760 °C.

Fig. 2. Creep tests at 760 °C of Fe–20Cr–30Ni–2Nb–5Al after annealing for 2.4 h at 800 °C.

are represented by a different color on Fig. 3.

In order to determine if the secondary creep rates were changing as a function of time, the creep rates were determined for intervals corresponding to the creep test times. Creep rates were determined by performing a least squares linear regression of creep strain versus time over the interval. These intervals are: from the start of secondary creep (approximately 35 h) to 250 h, 250 h–500 h, 1000 h–2000 h, 2000 h–3000 h, and 3000 h–4000 h. The creep rate was then averaged for each interval over all of the tests that ran for that length of time. The results are shown graphically in Fig. 4, which plots the strain rate vs total strain for creep of the alloy. The creep time corresponding to each strain is marked on the plot. It is clear that the creep rate continuously decreases from the first time interval (35–250 h) with a creep rate of 2.0×10^{-9} s^{-1} until the fourth time interval (1000–2000 h) with a creep rate of 2.8×10^{-10} s^{-1}. After 2000 h, the creep rate begins to slightly increase with the 2000–3000 h and 3000–4000 h intervals exhibiting creep rates of 5.8×10^{-10} s^{-1} and 4.7×10^{-10} s^{-1}, respectively. This, however, is still a significantly lower creep rate than seen in the intervals from 35 to 250 h and 250–500 h. The minimum strain rate occurs at a strain of approximately 1.58%, corresponding to a time of 2000 h. These results are similar to the creep study performed on another AFA alloy,

which showed that within the secondary creep regime the creep rate initially decreased before increasing again [19].

SEM imaging was used to analyze the microstructure after each creep test. BSE images for each creep-tested specimen are shown in Fig. 5. Fig. 5 shows how the precipitates in the matrix increase in size and volume fraction during creep, and how the GB coverage by precipitates correspondingly increases during creep. These data are enumerated in. Table 1, which quantifies the evolution of matrix precipitates, and in Table 2, which shows the evolution of GB coverage by each precipitate. After the 2.4 h anneal, only very fine Laves phase precipitates exist in the matrix and the GB coverage by both Laves and B2 phase precipitates is 35%. During creep, the Laves phase matrix precipitates grow and increase in volume fraction – eventually reaching 372 nm in average equivalent diameter and 3.1% volume fraction after 4000 h. The B2 phase precipitated in the matrix during creep, eventually reaching a similar size to the Laves phase precipitates. However, the volume fraction of B2 precipitates was always much less than that of the Laves precipitates. After 4000 h creep, the B2 matrix precipitates were 395 nm in average equivalent diameter and reached a 0.6% volume fraction. The GB coverage by both the Laves and B2 phases increased throughout the creep tests, with the B2 phase growing faster to reach a similar percent
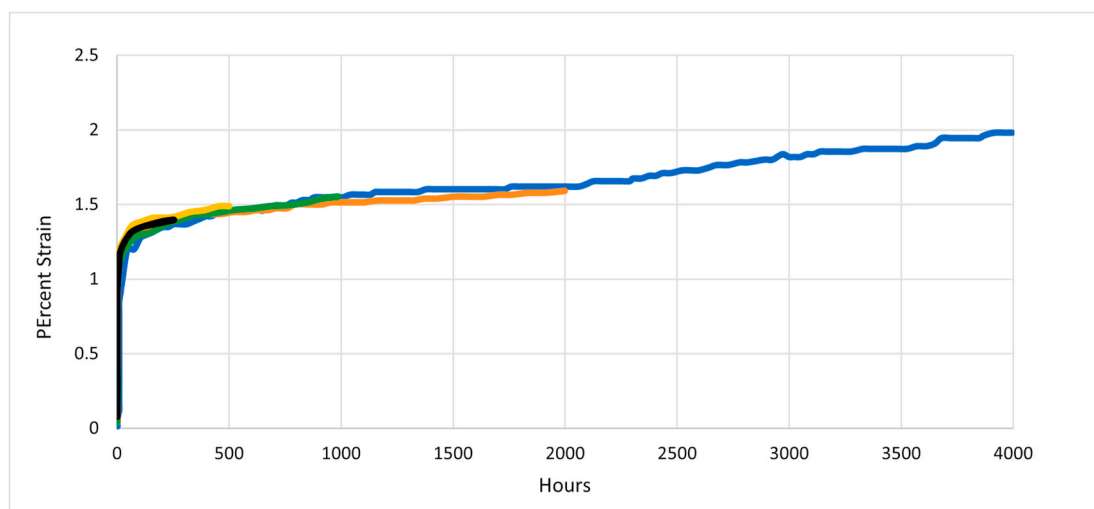

Fig. 3. Creep tests at 760 °C and 45 MPa for 250 h (black), 500 h (yellow), 1000 h (green), 2000 h (orange), and 4000 h (blue) of Fe–20Cr–30Ni–2Nb–5Al after annealing for 2.4 h at 800 °C. (For interpretation of the references to color in this figure legend, the reader is referred to the Web version of this article.)
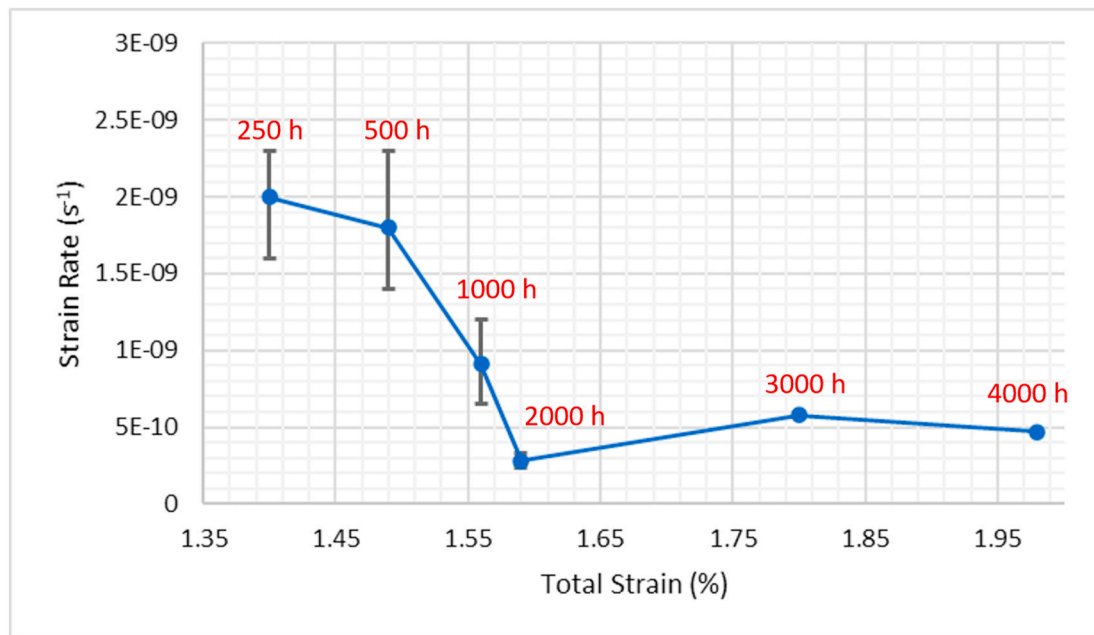
Fig. 4. Strain rate vs total strain for creep of Fe–20Cr–30Ni–2Nb–5Al at 760 °C and 45 MPa during secondary creep. The creep times corresponding to each strain are marked on the plot. The error bars represent the maximum strain rate recorded for each interval. The 3000 h and 4000 h only had one test run for that length of time, and thus no error bars are included. Note that the error bar for the 2000 h data is very small.
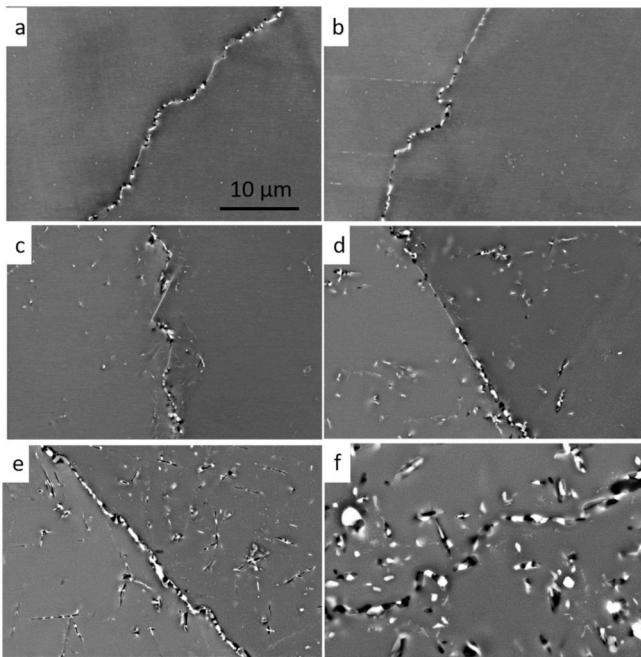

Fig. 5. SEM BSE images of Fe–20Cr–30Ni–2Nb–5Al after a) before testing, b) crept for 250 h, c) crept for 500 h, d) crept for 1000 h, e) crept for 2000h, and f) crept for 4000 h. Note the large alternating Laves and B2 precipitates along the grain boundaries.

Table 1

Evolution of Fe–20Cr–30Ni–2Nb–5Al matrix precipitates after creep for various times after creep at 45 MPa at 760 °C.

Creep Time (h)	Laves		B2		Total Volume Fraction (%)
	Average Size (nm)	Volume Fraction (%)	Average Size (nm)	Volume Fraction (%)	
0	<100	0.1 ± 0.04	0	0	0.1 ± 0.04
250	121 ± 19	0.1 ± 0.03	<100	<0.1	0.2 ± 0.04
500	185 ± 13	0.2 ± 0.03	155 ± 17	0.1 ± 0.02	0.3 ± 0.05
1000	203 ± 27	0.5 ± 0.05	191 ± 30	0.4 ± 0.08	0.9 ± 0.10
2000	309 ± 88	3.0 ± 0.98	297 ± 95	0.5 ± 0.31	3.5 ± 1.11
4000	372 ± 102	3.1 ± 0.89	395 ± 142	0.6 ± 0.22	3.7 ± 1.02

Table 2

Evolution of Fe–20Cr–30Ni–2Nb–5Al grain boundaries after creep for various times after creep at 45 MPa at 760 °C.

Creep Time (h)	GB Area Fraction Coverage%		
	Laves	B2	Total
0	22 ± 1	13 ± 2	35 ± 2
250	27 ± 6	15 ± 1	42 ± 6
500	31 ± 8	22 ± 7	53 ± 7
1000	35 ± 2	26 ± 5	61 ± 6
2000	42 ± 6	34 ± 13	76 ± 7
4000	43 ± 5	37 ± 9	80 ± 9

coverage as the Laves phase. After the 4000 h creep test, the Laves phase covered 43% and the B2 phase covered 37% of the GBs for a total GB coverage of 80%.

Additional images from the 4000 h creep test are shown in Fig. 6. Fig. 6a shows a lower magnification image of the microstructure after creep. Three features are worth noting. First, even at long creep times there was no cracking observed either along the GB, or through the GB precipitates. Second, the Laves and B2 precipitates tend to co-precipitate

in the matrix. Third, the Laves and B2 phases alternate along the entire length of the GBs. Fig. 6b is a higher magnification image of the same sample, which also shows several interesting features. First, very small $L1_2$ precipitates, which appear as white speckles, are visible in the matrix: these are only visible in SEM images after long creep times. Second, a PFZ is present along the GB. The PFZ runs the length of the GB but varies in width. The PFZ was only noticeable at long creep times ($\geq$2000 h).

While the SEM is useful for imaging the larger precipitates (Laves and B2) and the GBs, it is not useful for imaging the smaller $L1_2$
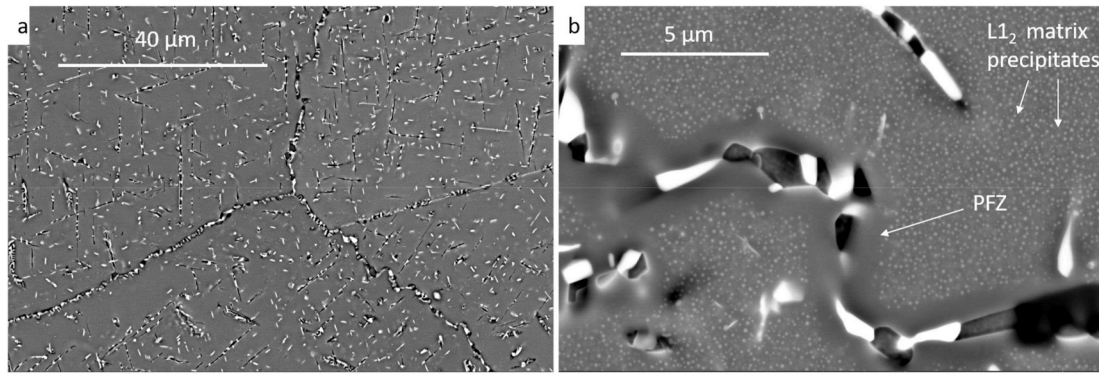
Fig. 6. SEM BSE images of Fe–20Cr–30Ni–2Nb–5Al after creep at 760 °C and 45 MPa for 4000 h. The small light areas in the matrix in (b) are $L1_2$ precipitates.

precipitates as they are too small to accurately measure. Thus, TEM bright-field (BF) imaging was used to image the $L1_2$ precipitates. Images for each creep time are shown in Fig. 7. The average size and volume fraction of the $L1_2$ precipitates are tabulated in Table 3. Prior to creep testing, there are no $L1_2$ precipitates in the microstructure. During the creep tests, the $L1_2$ precipitates nucleate and then grow in both size and volume fraction. After the 2000 h test, the average size is 46 nm and the volume fraction is 4.8%. After 4000 h, the average size has stabilized at 45 nm but the volume fraction continued to grow to 5.4%.

Fig. 8, Fig. 9, and Fig. 10 are graphical summaries of the precipitate

Table 3
Evolution of Fe–20Cr–30Ni–2Nb–5Al $L1_2$ precipitates after creep at 760 °C and 45 MPa for various times after annealing at 800 °C for 2.4 h.

Time (h)	Average Diameter (nm)	Volume Fraction (%)
0	0	0
250	18 ± 3	0.5 ± 0.35
500	26 ± 3	1.9 ± 0.58
1000	33 ± 2	4.5 ± 0.65
2000	46 ± 4	4.8 ± 0.75
4000	45 ± 7	5.4 ± 1.25

size, volume fraction, and GB coverage vs creep time, respectively. The shaded regions in these plots represent 95% confidence intervals.

Fig. 11 shows TEM images from this alloy after 2000 h of creep at 760 °C and 45 MPa. Fig. 11a and b display bright-field images of dislocations by-passing particles by climb and bowing between $L1_2$ precipitates, while Fig. 11c and d display a bright-field and weak-beam dark-field image of dislocations cutting through a $L1_2$ precipitate.

The 75 MPa and 760 °C creep test was the only test in this study performed until failure. The fracture surface of this sample after failure was imaged in the SEM, see Fig. 12. The jagged lines on the fracture surface clearly indicate that the sample fractured in an intergranular manner, i.e. along the grain boundaries.

Additionally, room temperature hardness tests were performed after each creep time. These results are shown in Fig. 13. The hardness quickly increases after the initial 250 h of creep, and the stabilizes and the hardness stays within the bounds of error for up to 4000 h of creep.

4. Discussion

A plot of precipitate size versus time$^{1/3}$, see Fig. 14a, produces a linear fit for each type of precipitate in the matrix. This suggests that the coarsening of the all the matrix precipitates is following the Ostwald ripening law. Studies of other AFA alloys also found that the $L1_2$ matrix precipitates followed the Ostwald ripening law [19,25]. Fig. 14b shows a plot of precipitate size cubed versus time. This plot is useful for determining the coarsening rate constant, K, which is the slope of the line in this plot. The Laves phase and B2 precipitates have very similar coarsening rate constants, with values of 3.7×10^{-27} and 4.4×10^{-27} m^3/s, respectively. This is similar to the calculated rate coarsening constant of 2.41×10^{-27} m^3/s for Laves phase precipitates in a different AFA alloy at 750 °C [26]. The $L1_2$ precipitates display a coarsening rate constant several orders of magnitude lower than the Laves phase and B2 precipitates, at 7.0×10^{-30} m^3/s, showing a much better resistance to coarsening. This is similar to the reported coarsening constant of 8.5×10^{-30} m^3/s for $L1_2$ precipitates in a different AFA alloy at 750 °C [25]. It is interesting to note that the B2 and $L1_2$ precipitates have a quite similar chemistry, meaning that the coefficient of diffusion will be similar. This suggests that the main reason for the $L1_2$ precipitates having a better
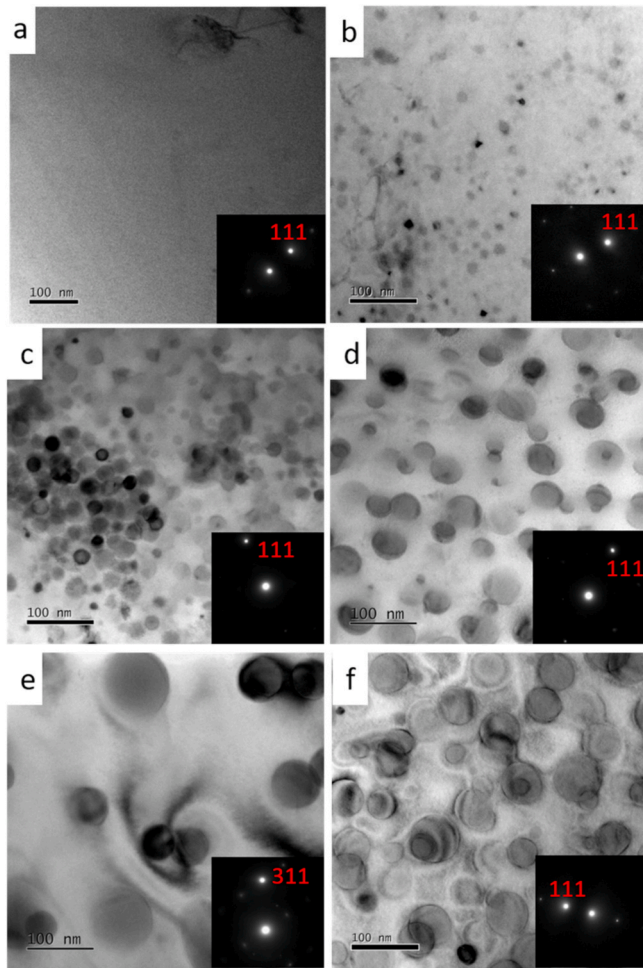

Fig. 7. TEM bright-field images of Fe–20Cr–30Ni–2Nb–5Al after a) 2.4 h, 800 °C anneal only, b) creep for 250 h, c) creep for 500 h, d) creep for 1000 h, e) creep for 2000 h, and f) creep for 4000 h.
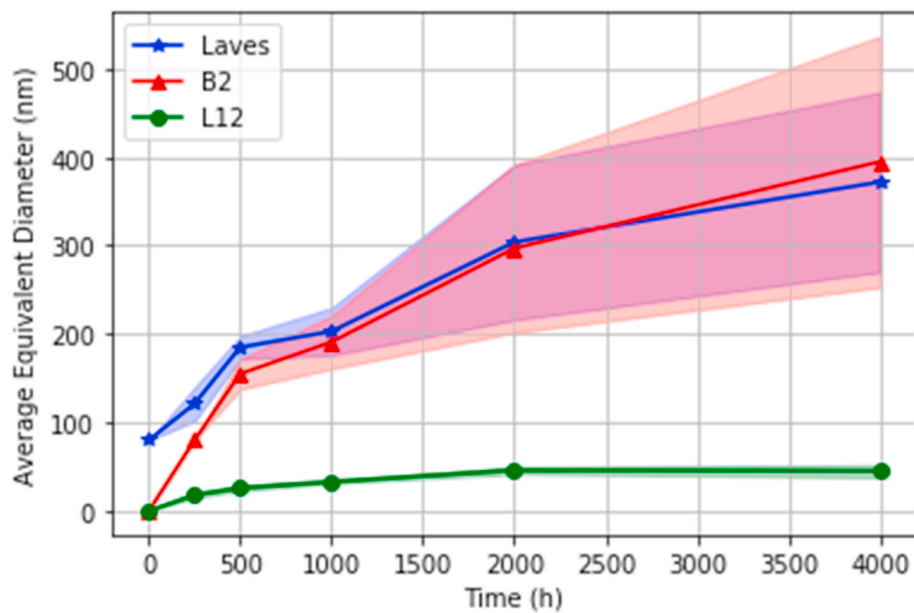
Fig. 8. Average matrix precipitate size after different creep times at 760 °C for Fe–20Cr–30Ni–2Nb–5Al. The shaded areas represent 95% confidence intervals.
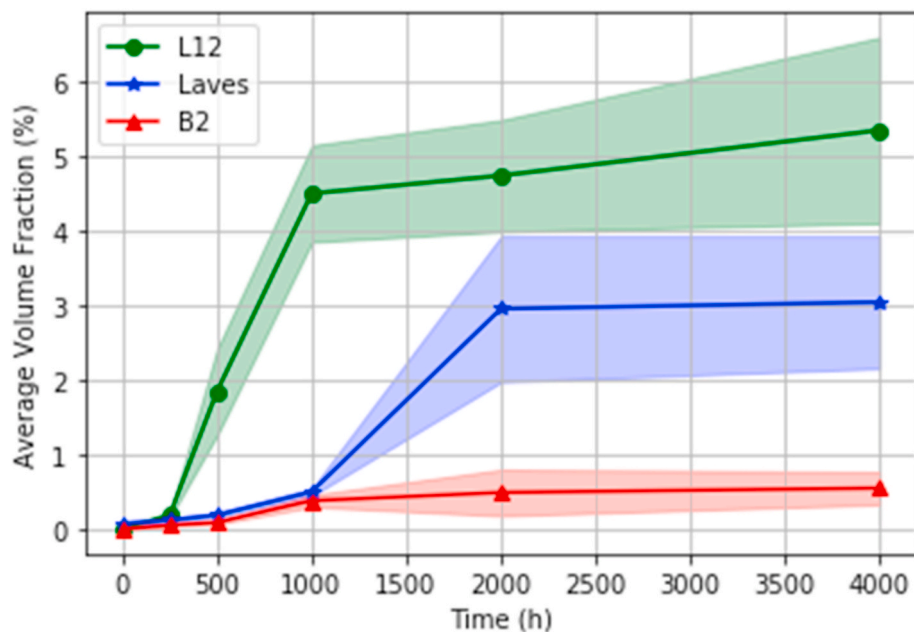

Fig. 9. Matrix precipitate volume fraction after different creep times at 760 °C for Fe–20Cr–30Ni–2Nb–5Al. The shaded areas represent 95% confidence intervals.

resistance to coarsening is because of differences in the specific interfacial energy or in the lattice misfit.

Analysis of the creep rate showed that the secondary creep rate was clearly changing with respect to time: initially the creep rate decreased until around 2000 h of creep, after which the creep rate began to slightly increase. Analyzing the microstructure of the alloy with respect to time provides insight into the cause of this behavior. Let's start by determining which microstructure features could be contributing to the strengthening up to 2000 h of creep. Preliminary creep and high temperature tensile tests performed by Baker et al. [20] on this alloy found that very fine Laves phase precipitates (around 100 nm in average equivalent diameter) resulted in increased high temperature tensile and creep strength at 760 °C. As the Laves phase precipitates further increased in size (and as the B2 phase precipitates nucleated and grew) the high temperature strength decreased. In this study, the Laves phase

precipitates were originally very fine (<100 nm average equivalent diameter) with no B2 precipitates in the matrix. After 250 h of creep the Laves precipitates had an average equivalent diameter of 123 nm and the B2 precipitates were still very small (average equivalent diameter < 100 nm). Already, the precipitates were reaching sizes that resulted in lower high temperature strength. After 500 h of creep, the Laves precipitates grew to 185 nm average equivalent diameter and the B2 precipitates grew to 155 nm average equivalent diameter. Thus, it is very likely that the Laves phase precipitates are not contributing to the decreasing creep rate – in fact, as the Laves and B2 precipitates coarsen they likely decrease the strength of the material. These results agree with findings by Yamamoto et al. in their study of a different AFA alloy that the size and volume fraction of Laves phase precipitates strongly effect the strengthening properties of the Laves phase – in fact, they reported similar sizes and concluded that stabilizing these precipitates to sizes of
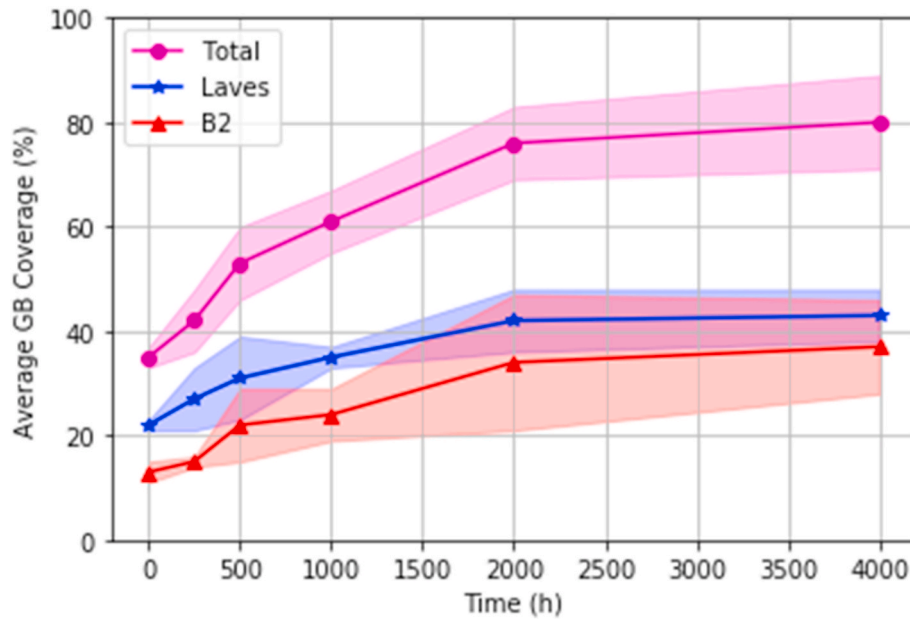
Fig. 10. Grain boundary area coverage after different creep times at 760 °C for Fe–20Cr–30Ni–2Nb–5Al. The shaded areas represent 95% confidence intervals.
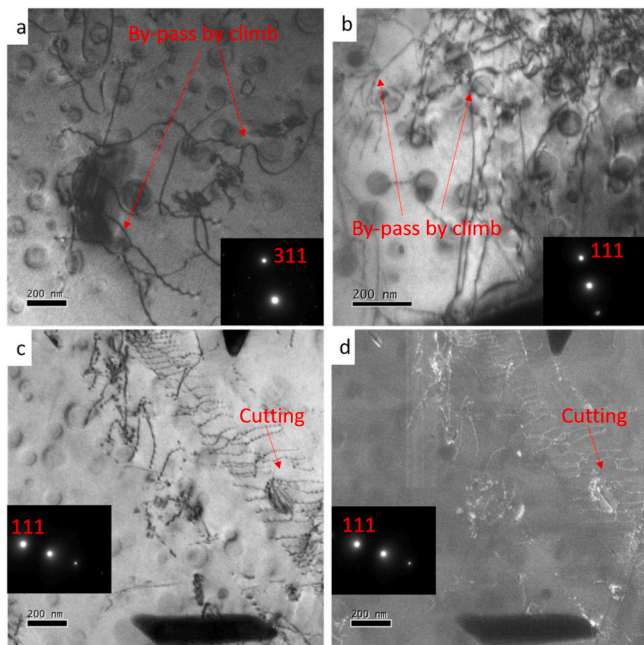

Fig. 11. TEM images of Fe–20Cr–30Ni–2Nb–5Al after creep for 2000 h at 760 °C and 45 MPa. a) BF image showing by-pass by climb of $L1_2$ precipitates, b) BF image showing by-pass by climb of $L1_2$ precipitates, c) BF image showing cutting of $L1_2$ precipitates, and d) weak-beam dark field image showing the same area as c, using the g-3g condition.

100 nm or less would be needed to maximize the strength of the alloy [10].

Another possible explanation for the increase in creep resistance is the nucleation and then growth of the $L1_2$ precipitates. It is commonly reported that $L1_2$ precipitates provide strengthening at high temperatures, particularly when they are on the scale of 100 nm diameter or less [10,27–29]. After the 2.4 h 800 °C anneal (and before creep) no $L1_2$ precipitates were present. After creep for 250 h at 760 °C and 45 MPa the $L1_2$ precipitates had an average diameter of 18 nm and a volume fraction of 0.49%. After creep for 2000 h, the precipitates had grown to 46 nm in

average diameter with a 4.75% volume fraction. After this, the size appears to stabilize but the volume fraction continues to increase. After creep for 4000 h, the precipitates were 45 nm in average diameter and the volume fraction was 6.34%. We can estimate how much strengthening these $L1_2$ precipitates are providing by determining the deformation mechanism. The deformation behavior of precipitation-hardened alloys can be divided into three categories – particle cutting (in which the dislocations cut through the particle, generally when the particle is coherent with the interface), Orowan looping (in which the dislocations loop tightly around the precipitates), and at elevated temperature by-passing the particles by climb (in which the dislocations climb past precipitates, but do not have the required stress to create Orowan loops) [30,31]. The stress necessary to operate each mechanism depends on the particle size and spacing, but in general the cutting mechanism will dominate at smaller particle sizes and by-pass by climb or Orowan looping mechanisms will dominate at larger particle sizes [30]. TEM imaging of this alloy after creep showed that by-passing particles by climb was the primary mechanism, although some instances of particle cutting were also found.

Since by-pass by climb is the primary mechanism observed, we can calculate the stress needed to operate that mechanism after each creep length. This value will provide a good estimate of the strengthening effect of the $L1_2$ precipitates at each creep time. The stress needed to by-pass particles by general climb can be estimated as approximately 0.05 * τ_0 (where τ_0 is the Orowan stress) [32]. The stress needed to operate the Orowan looping mechanism is calculated as:

$$\tau_0 = \frac{Gb}{\lambda - 2r}$$

Where G is the shear modulus, b is the Burgers vector, λ is the mean interparticle spacing, and r is the mean particle radius. G is approximately 50 GPa and b is approximately 0.253 nm for AFA alloys. λ and r are both easily calculated from the average size and volume fraction. Table 4 shows the average size as well as Orowan stress for each creep time. Initially, the Orowan stress is 0 MPa because there are no $L1_2$ precipitates in the microstructure. The Orowan stress then steadily increases, reaching 303 MPa after 1000 h of creep. The stress needed to by-pass particles by local climb is proportional to the Orowan stress, and thus will increase as Orowan stress increases. The Orowan stress then slightly decreases as the precipitates continue to coarsen. Based on these
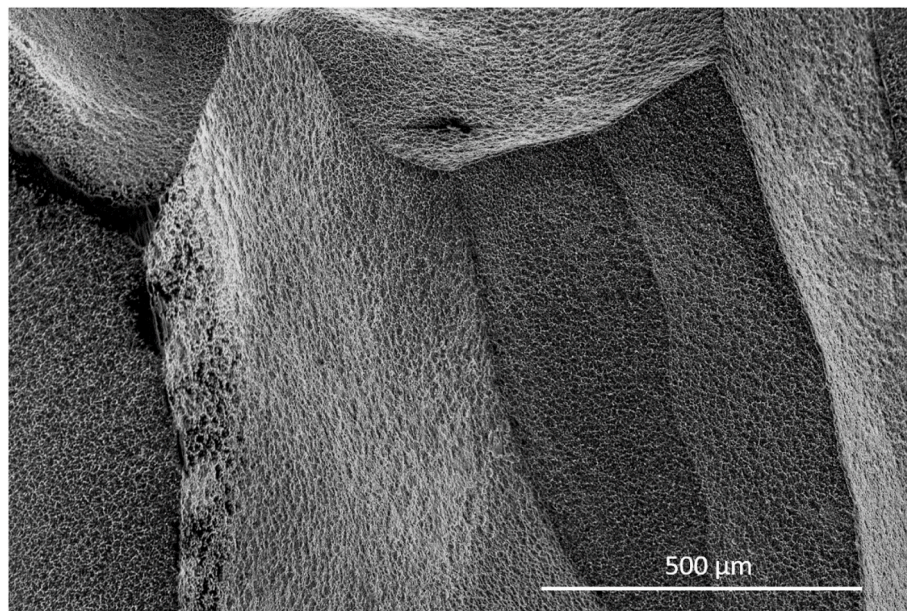
Fig. 12. SEM image of the fracture surface of Fe–20Cr–30Ni–2Nb–5Al after annealing for 2.4 h at 800 °C, followed by creeping until failure at 760 °C and 75 MPa.
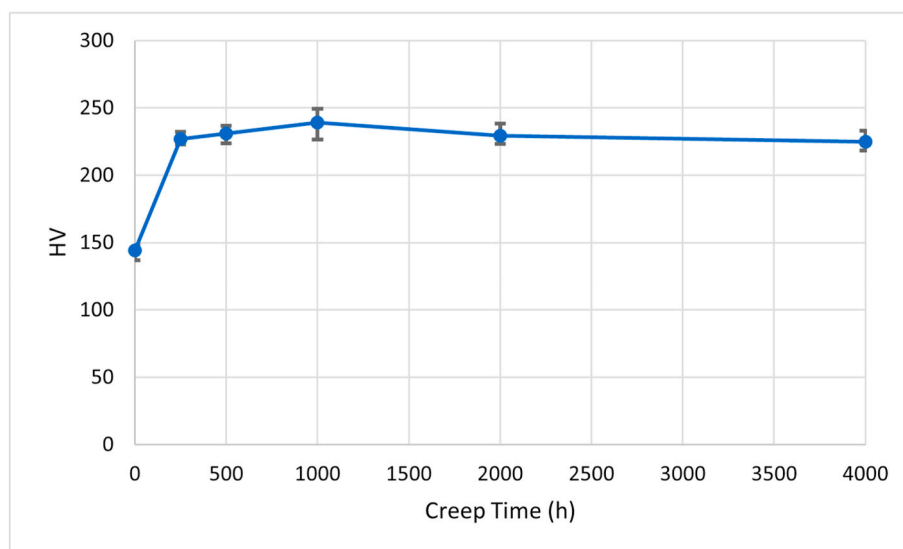

Fig. 13. Vickers Hardness (HV) of Fe–20Cr–30Ni–2Nb–5Al after annealing at 800 °C for 2.4 h, followed by creep at 760 °C and 45 MPa for different lengths of time. The error bars represent the maximum and minimum hardness value for each condition.

results, the L1$_2$ precipitates are clearly providing significant strengthening to the alloy – and thus decreasing the creep rate. The Orowan stress shows roughly similar trends to the hardness values in Fig. 13, with a large increase at the beginning of creep and then remaining similar for the remainder of the creep testing.

The final possibility for the decreasing creep rate is strengthening of the GBs by precipitate coverage. Studies have shown that in alloys where the GBs are covered by Laves phase precipitates, there is GB strengthening effect in which the precipitates prevent GB sliding [15,33]. However, in this case it seems that this would play a smaller role in strengthening the alloy. Fig. 15 shows a log-log plot of stress versus strain for creep at 760 °C. In order to deal with the changing creep rates, creep data were taken from the same length of time for each test – from the start of secondary creep to 2000 h. The slope of this line, n, is the exponent in the power-law creep equation. This exponent can be used to predict the deformation regime that the creep is occurring in. When n =

1, creep is in the diffusion creep or GB sliding regime [34]. When n = 3 or great, creep is in the dislocation creep regime [34]. Here, n = 2.7, implying that creep is likely occurring in the dislocation creep regime. However, it is still likely that the GB precipitates are reducing GB sliding and, in turn, helping to reduce the creep rate. However, as mentioned previously, preliminary work on Fe–20Cr–30Ni–2Nb–5Al indicated that GB coverage seemed to have little effect on the strength at 760 °C after approximately 42% coverage. In these creep tests, 42% coverage was reached after 250 h of creep. The majority of the creep strengthening appears to occur in the 500–2000 h range, suggesting it is unlikely that the GB coverage is significantly increasing the creep strength.

To check this, the results of this study can be compared with the findings of Tarigan et al. which determined that the creep rate decreases linearly with increased GB coverage [15]. The initial creep study on Fe–20Cr–30Ni–2Nb–5Al by Baker et al. found that creep strength decreased with increased GB coverage [20], which is at odds with the
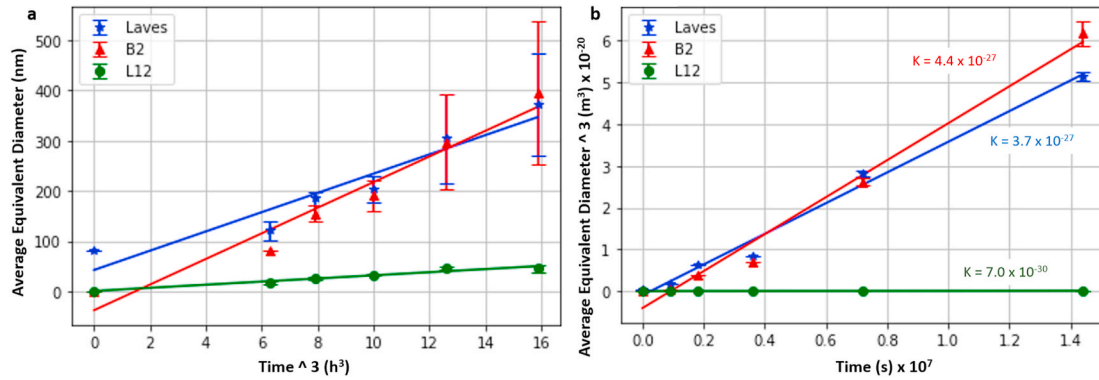
Fig. 14. Average equivalent diameter of different precipitates vs time after different creep times at 760 °C for Fe–20Cr–30Ni–2Nb–5Al. The solid lines represent least squares regression lines. Error bars represent 95% confidence intervals for the size.

Table 4
Orowan stress for L1$_2$ precipitates in Fe–20Cr–30Ni–2Nb–5Al during creep at 760 °C and 45 MPa after annealing for 2.4 h at 800 °C.

Time (h)	Average Diameter (nm)	τ (MPa)
0	0	0
250	18 ± 3	188 ± 17
500	26 ± 3	238 ± 23
1000	33 ± 2	303 ± 21
2000	46 ± 4	224 ± 29
4000	45 ± 7	275 ± 31

findings of Tarigan et al. However, it is important to note that the matrix precipitates were changing in size and volume fraction in the study by Baker et al. and the model proposed by Tarigan et al. does not take into account the effect of matrix precipitates. For the present study, the GB coverage for the start of each time interval is plotted against the creep rate for that interval, see Fig. 16. This plot results in a fairly good linear fit for the first 2000 h of creep, but then the creep rate increases after 2000 h while the GB coverage continues to increase. This plot, coupled with the preliminary creep testing by Baker et al. suggests that the matrix precipitates control the creep strength more than the GB precipitates.

Zhang et al. developed a model for GB strengthening in Fe–15Cr–25Ni alloys with carbides on the GBs in the dislocation creep regime [35]. In this model, they incorporate an obstacle stress term describes how dislocations pile-up at the GBs, creating a difference in local stresses. The strains near the GB and in the matrix are then matched in order to determine the equation for this obstacle stress term. This obstacle stress is in addition to the threshold stress needed to overcome precipitates in the matrix, such as in the model proposed by Rosler and Arzt [36], meaning that this model takes into account both precipitates in the matrix and on the GBs. This model was shown to fit experimental results well. The mode is shown below.

$$\dot{\varepsilon} = (\sigma - \sigma_{th} - \sigma_{BO})^n \exp\left(-\frac{Q}{RT}\right)$$

Where σ_{th} is the threshold stress for the matrix precipitates, σ_{BO} is the obstacle stress for the GB precipitates, Q is the activation energy for creep, R is the gas constant, and T is the temperature. σ_{BO} is calculated as:

$$\sigma_{BO} = (m)(2KGb/d)^{\frac{1}{2}}(\sigma)^{\frac{1}{2}}\left(1 - \frac{\sigma_{th}}{\sigma}\right)$$

Where m is the GB fraction coverage, K is a constant that is usually approximately 23, and d is grain size. These variables can be easily calculated or approximated. The threshold stress in the matrix was calculated earlier in this paper from L1$_2$ precipitates. The activation energy for creep can be assumed to be approximately the same as the self-diffusion of Fe in austenite, which is 280 kJ/mol [37]. The average
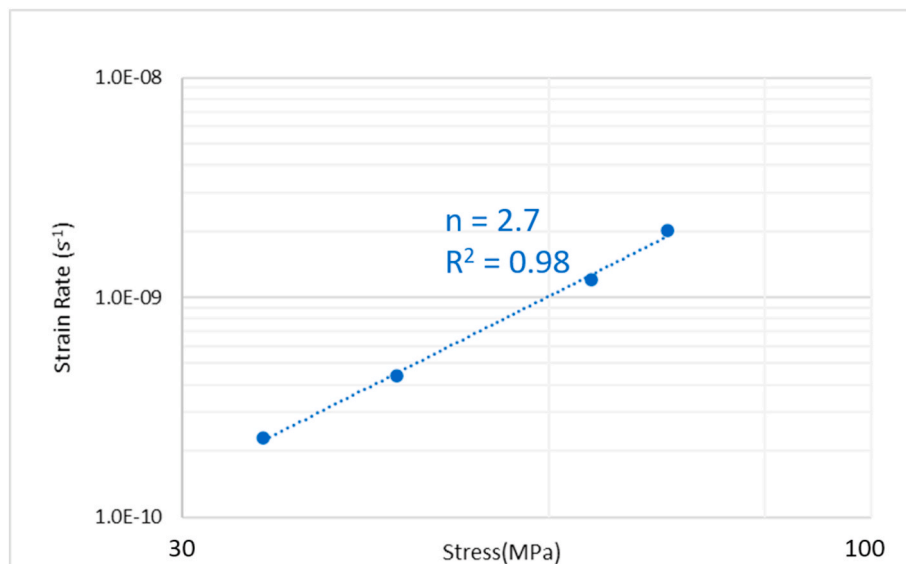

Fig. 15. Log-log plot of stress vs strain for creep of Fe–20Cr–30Ni–2Nb–5Al at 760 °C.
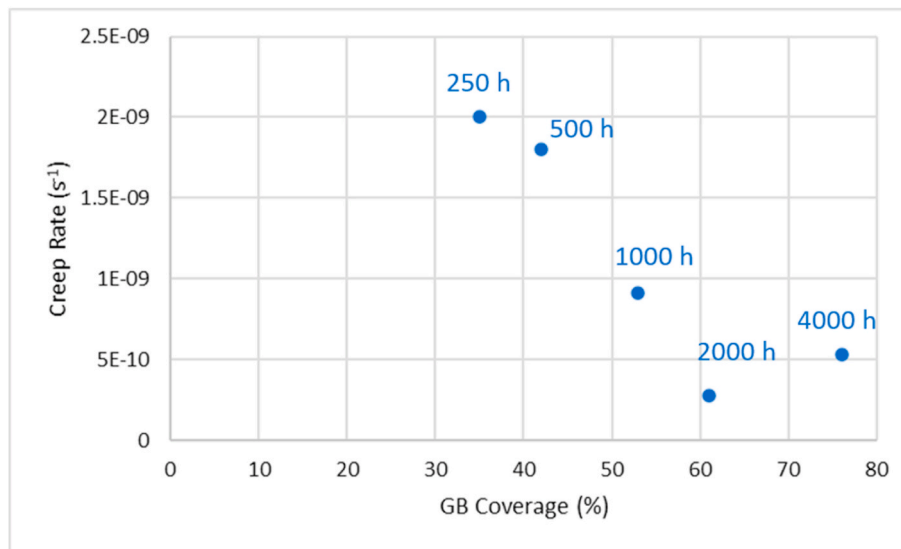
Fig. 16. Creep rate vs grain boundary coverage, for creep of Fe–20Cr–30Ni–2Nb–5Al at 760 °C and 45 MPa.

grain size is approximately 450 μm average equivalent circle diameter. The creep strain can then be plotted against the effective stress, $\sigma - \sigma_{th} - \sigma_{BO}$, which should result in a linear fit, see Fig. 17. This plot shows a fairly strong linear relationship, suggesting that this model represents the creep deformation well. However, it is important to note that the model does not take into account the PFZ that forms at long creep times, and also does not account for the Laves phase and B2 precipitates in the matrix.

After creep for 2000 h, the creep rate slightly increased. There are several possible explanations for this, all of which likely play a part. First, as discussed earlier, as the Laves and B2 phase precipitates coarsen they have been shown to weaken the material. After creep for 2000 h, the Laves and B2 phase precipitates have become much larger. Second, the $L1_2$ precipitates coarsen over time and as a result there is a slight decrease in the Orowan stress – and this, the stress needed to climb past particles. While these precipitates are still strengthening, they are not strengthening as effectively. Third, a PFZ begins to form after 2000 h. In an alloy strengthened by precipitates, the PFZ is likely much weaker than the matrix. Studies on the effect of a PFZ in $L1_2$ strengthened nickel-base super alloys suggests a PFZ would reduce the yield strength of the

material if the PFZ was larger than 1.7*(λ-r) [38,39]. In this study, this value is 132 nm after 4000 h creep. Measurement of the PFZ size after 4000 h creep shows that it varies between 500 nm and 1 μm. This is significantly larger than 132 nm, and thus it is likely that the PFZ is reducing the strength. A previous study on an AFA alloy found that after failure at high temperature, there was significant cracking either along the GB or the PFZ – which indicated that the PFZ was a possible weak area in which the material failed [40]. While similar behavior was not observed here, the fracture was intergranular which suggests that the PFZ or GB was still the weak point in the microstructure. However, it is not clear if the failure is due to the PFZ, the coarse precipitates covering the GBs, or other reasons.

5. Conclusions

The creep behavior of the AFA model alloy Fe–20Cr–30Ni–2Nb–5Al at 760 °C was studied. Creep tests were run for different times in order to determine how the microstructure evolved during creep and what effect this had on the creep rate. The findings can be summarized as follows:
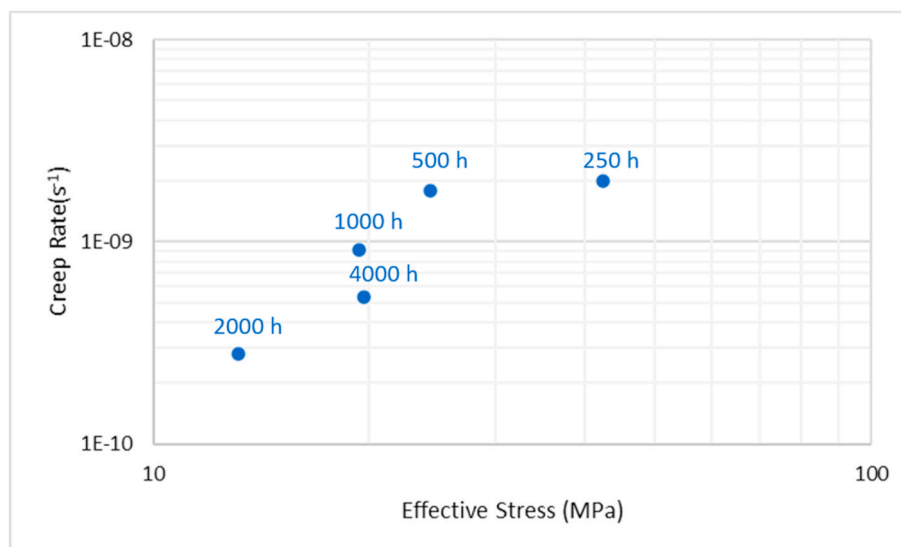

Fig. 17. Creep rate vs effective stress, for creep of Fe–20Cr–30Ni–2Nb–5Al at 760 °C and 45 MPa.

1. The creep rate changed as the microstructure evolved during creep.
2. Previous work showed that coarsening of the Laves phase and B2 precipitates decreased the strength [20], thus it is likely that the coarsening of the Laves Fe_2Nb and B2 NiAl matrix precipitates during creep decreased the creep strength. Stabilizing the size of these precipitates at smaller sizes would help to increase the creep strength of the alloy.
3. The nucleation of $L1_2$ Ni_3Al precipitates greatly increased the creep strength. Optimizing the size and spacing would provide the most effective strengthening.
4. While GB strengthening by coverage with Laves and B2 precipitates may have helped increase the creep strength, it is likely that it played a much smaller role than the strengthening by $L1_2$ precipitates. Further research into the GB strengthening mechanism would lead to a better understanding of its role.
5. The PFZ likely weakened the material along the GBs, but cracking was not seen along the GBs as reported in work on other AFA alloys. However, the alloy still failed with an intergranular fracture mode, suggesting that the PFZ or GB is the weakest part of the microstructure. More research needs to be done to better understand the role of the PFZ on GB strength.

6. Data availability

The raw/processed data required to reproduce these findings cannot be shared at this time as the data also forms part of an ongoing study.

CRediT authorship contribution statement

Andrew Peterson: Conceptualization, Methodology, Investigation, Writing - original draft, Visualization. **Ian Baker:** Conceptualization, Resources, Writing - review & editing, Funding acquisition.

Declaration of competing interest

The authors declare that they have no known competing financial interests or personal relationships that could have appeared to influence the work reported in this paper.

Acknowledgements

References

[1] R. Viswanathan, J.F. Henry, J. Tanzosh, G. Stanko, J. Shingledecker, B. Vitalis, R. Purgert, U.S. Program on materials technology for ultra-supercritical coal power plants, J. Mater. Eng. Perform. 14 (2005) 281–292, https://doi.org/10.1361/10599490524039.

[2] R. Viswanathan, W. Bakker, Materials for ultrasupercritical coal power plants - boiler materials: Part 1, J. Mater. Eng. Perform. 10 (2001) 81–95, https://doi.org/10.1361/105994901770345394.

[3] J.P. Shingledecker, I.G. Wright, Evaluation of the materials technology required for a 760°C power steam boiler. https://www.osti.gov/biblio/931631, 2006 (accessed June 26, 2019).

[4] M. Takeyama, Novel concept of austenitic heat resistant steels strengthened by intermetallics, Mater. Sci. Forum 539–543 (2007) 3012–3017. https://doi.org/10.4028/www.scientific.net/MSF.539-543.3012.

[5] M.P. Brady, Y. Yamamoto, M.L. Santella, P.J. Maziasz, B.A. Pint, C.T. Liu, Z.P. Lu, H. Bei, The development of alumina-forming austenitic stainless steels for high-temperature structural use, J. Occup. Med. 60 (2008) 12–18, https://doi.org/10.1007/s11837-008-0083-2.

[6] M.P. Brady, Y. Yamamoto, M.L. Santella, B.A. Pint, Effects of minor alloy additions and oxidation temperature on protective alumina scale formation in creep-resistant austenitic stainless steels, Scripta Mater. 57 (2007) 1117–1120, https://doi.org/10.1016/J.SCRIPTAMAT.2007.08.032.

[7] B.A. Pint, J.P. Shingledecker, M.P. Brady, P.J. Maziasz, Alumina-forming austenitic alloys for advanced recuperators, Turbo Expo 2007, ASME, https://doi.org/10.1115/GT2007-27916, 2007, 3, 995-1002.

[8] Y. Yamamoto, M.P. Brady, Z.P. Lu, P.J. Maziasz, C.T. Liu, B.A. Pint, K.L. More, H.M. Meyer, E.A. Payzant, Creep-resistant, Al2O3-forming austenitic stainless steels, Science 316 (2007) 433–436, https://doi.org/10.1126/science.1137711.

[9] Y. Yamamoto, M.P. Brady, Z.P. Lu, C.T. Liu, M. Takeyama, P.J. Maziasz, B.A. Pint, Alumina-forming austenitic stainless steels strengthened by laves phase and MC carbide precipitates, Metall. Mater. Trans. 38 (2007) 2737–2746, https://doi.org/10.1007/s11661-007-9319-y.

[10] Y. Yamamoto, M. Takeyama, Z.P. Lu, C.T. Liu, N.D. Evans, P.J. Maziasz, M.P. Brady, Alloying effects on creep and oxidation resistance of austenitic stainless steel alloys employing intermetallic precipitates, Intermetallics 16 (2008) 453–462, https://doi.org/10.1016/J.INTERMET.2007.12.005.

[11] Y. Yamamoto, M.P. Brady, M.L. Santella, H. Bei, P.J. Maziasz, B.A. Pint, Overview of strategies for high-temperature creep and oxidation resistance of alumina-forming austenitic stainless steels, Metall. Mater. Trans. 42 (2011) 922–931, https://doi.org/10.1007/s11661-010-0295-2.

[12] M.P. Brady, J. Magee, Y. Yamamoto, D. Helmick, L. Wang, Co-optimization of wrought alumina-forming austenitic stainless steel composition ranges for high-temperature creep and oxidation/corrosion resistance, Mater. Sci. Eng. 590 (2014) 101–115, https://doi.org/10.1016/J.MSEA.2013.10.014.

[13] P. Kofstad, Defects and transport properties of metal oxides, Oxid. Metals 44 (1995) 3–27, https://doi.org/10.1007/BF01046721.

[14] U. Heubner, Nickel Alloys, Marcel Dekker, 1998. https://books.google.com/books/about/Nickel_Alloys.html?id=-ufvbPfm3BUC. accessed June 29, 2019.

[15] I. Tarigan, K. Kurata, N. Takata, T. Matsuo, M. Takeyama, Novel concept of creep strengthening mechanism using grain boundary Fe_2Nb laves phase in austenitic heat resistant steel, MRS Proc 1295 (2011), https://doi.org/10.1557/opl.2011.558 mrsf10-1295-n06-03.

[16] D.Q. Zhou, X.Q. Xu, H.H. Mao, Y.F. Yan, T.G. Nieh, Z.P. Lu, Plastic flow behaviour in an alumina-forming austenitic stainless steel at elevated temperatures, Mater. Sci. Eng. 594 (2014) 246–252, https://doi.org/10.1016/j.msea.2013.11.021.

[17] B. Hu, I. Baker, The effect of thermo-mechanical treatment on the high temperature tensile behavior of an alumina-forming austenitic steel, Mater. Sci. Eng. 651 (2016) 795–804, https://doi.org/10.1016/j.msea.2015.11.036.

[18] B. Zhao, K. Chang, J. Fan, Z. Chen, X. Dong, L. Zhang, Annealing effects on precipitation and high-temperature properties of a Cu-containing alumina-forming austenitic steel, Mater. Lett. 176 (2016) 83–86, https://doi.org/10.1016/j.matlet.2016.04.110.

[19] H. Wen, B. Zhao, X. Dong, F. Sun, L. Zhang, A systematic investigation of precipitates in matrix and at grain boundaries in an alumina-forming austenitic steel during creep testing at 700 °C, Metall. Mater. Trans. A Phys. Metall. Mater. Sci. 51 (2020) 4186–4194, https://doi.org/10.1007/s11661-020-05848-4.

[20] I. Baker, N. Afonina, Z. Wang, M. Wu, Preliminary creep testing of the alumina-forming austenitic stainless steel Fe-20Cr-30Ni-2Nb-5Al, Mater. Sci. Eng. 718 (2018) 492–498, https://doi.org/10.1016/J.MSEA.2018.01.090.

[21] G. Trotter, I. Baker, Orientation relationships of Laves phase and NiAl particles in an AFA stainless steel, Philos. Mag. A 95 (2015) 4078–4094, https://doi.org/10.1080/14786435.2015.1111529.

[22] G. Trotter, I. Baker, The effect of aging on the microstructure and mechanical behavior of the alumina-forming austenitic stainless steel Fe–20Cr–30Ni–2Nb–5Al, Mater. Sci. Eng. 627 (2015) 270–276, https://doi.org/10.1016/j.msea.2014.12.072.

[23] G. Trotter, G. Rayner, I. Baker, P.R. Munroe, Accelerated precipitation in the AFA stainless steel Fe-20Cr-30Ni-2Nb-5Al via cold working, Intermetallics 53 (2014) 120–128, https://doi.org/10.1016/j.intermet.2014.04.018.

[24] F. Garofalo, O. Richmond, W.F. Domis, Design of apparatus for constant-stress or constant-load creep tests, J. Fluids Eng. Trans. ASME. 84 (1962) 287–293, https://doi.org/10.1115/1.3657303.

[25] G. Trotter, B. Hu, A.Y. Sun, R. Harder, M.K. Miller, L. Yao, I. Baker, Precipitation kinetics during aging of an alumina-forming austenitic stainless steel, Mater. Sci. Eng. 667 (2016) 147–155, https://doi.org/10.1016/j.msea.2016.04.081.

[26] W.X. Zhao, D.Q. Zhou, S.H. Jiang, H. Wang, Y. Wu, X.J. Liu, X.Z. Wang, Z.P. Lu, Ultrahigh stability and strong precipitation strengthening of nanosized NbC in alumina-forming austenitic stainless steels subjecting to long-term high-temperature exposure, Mater. Sci. Eng. 738 (2018) 295–307, https://doi.org/10.1016/j.msea.2018.09.081.

[27] B. Hu, G. Trotter, Z. Wang, S. Chen, Z. Cai, I. Baker, Effect of boron and carbon addition on microstructure and mechanical properties of the aged gamma-prime strengthened alumina-forming austenitic alloys, Intermetallics 90 (2017) 36–49, https://doi.org/10.1016/j.intermet.2017.06.011.

[28] Y. Yamamoto, G. Muralidharan, M.P. Brady, Development of L12-ordered Ni3(Al, Ti)-strengthened alumina-forming austenitic stainless steel alloys, Scripta Mater. 69 (2013) 816–819, https://doi.org/10.1016/J.SCRIPTAMAT.2013.09.005.

[29] B.B. Zhao, X.P. Dong, F. Sun, L.T. Zhang, Impact of L12-ordered precipitation on the strength of alumina-forming austenitic heat-resistant steels, Mater. Sci. Forum 941 (2018) 692–697. https://doi.org/10.4028/www.scientific.net/MSF.941.692.

[30] R. Lagneborg, B. Bergman, The stress/creep rate behaviour of precipitation-hardened alloys. https://doi.org/10.1179/030634576790431462, 2014.

[31] J. Zhang, Creep of second phase particles strengthened materials, in: High Temp. Deform. Fract. Mater., Elsevier, 2010, pp. 83–101, https://doi.org/10.1533/9780857090805.1.83.

[32] E. Arzt, M.F. Ashby, Threshold stresses in materials containing dispersed particles, Scripta Metall. 16 (1982) 1285–1290, https://doi.org/10.1016/0036-9748(82)90484-7.

[33] S.W. Chen, C. Zhang, Z.X. Xia, H. Ishikawa, Z.G. Yang, Precipitation behavior of Fe2Nb Laves phase on grain boundaries in austenitic heat resistant steels, Mater. Sci. Eng. 616 (2014) 183–188, https://doi.org/10.1016/J.MSEA.2014.07.104.

[34] T. Hyde, W. Sun, C. Hyde, Applied Creep Mechanics, McGraw-Hill Education, 2014.

[35] J.S. Zhang, P.E. Li, W.X. Chen, J.Z. Jin, Grain boundary precipitation strengthening in high temperature creep of Fe15Cr25Ni alloys, Scripta Metall. 23 (1989) 547–551, https://doi.org/10.1016/0036-9748(89)90449-3.

[36] J. Rösler, E. Arzt, The kinetics of dislocation climb over hard particles-I. Climb without attractive particle-dislocation interaction, Acta Metall. 36 (1988) 1043–1051, https://doi.org/10.1016/0001-6160(88)90158-7.

[37] M.F. Ashby, H.J. Frost, Deformation-mechanism Maps, Oxford Pergamon Press, 1982.

[38] T. Krol, D. Baither, E. Nembach, Quantification of the detrimental effects of precipitate free zones on the yield strength of a superalloy, Scripta Mater. 48 (2003) 1189–1194, https://doi.org/10.1016/S1359-6462(02)00566-3.

[39] D. Baither, T. Krol, E. Nembach, *In-situ* transmission electron microscopy study of dislocation processes at precipitate-free zones in a γ′-strengthened superalloy, Philos. Mag. A 83 (2003) 4011–4029, https://doi.org/10.1080/14786430310001603445.

[40] B. Hu, I. Baker, S.J. Kernion, Y. Yamamoto, M.P. Brady, Creep failure of a gamma prime-strengthened alumina-forming austenitic stainless steel, in: Adv. Mater. Technol. Foss. Power Plants - Proc. From 8th Int. Conf, 2016.